CrystEngComm

PAPER

View Article Online
View Journal | View Issue

Cite this: *CrystEngComm*, 2014, **16**, 3950

Effect of processing conditions on the crystallinity and structure of carbonated calcium hydroxyapatite (CHAp)

Edita Garskaite,*[a] Karlis-Agris Gross,*[b] Sung-Wei Yang,[c] Thomas Chung-Kuang Yang,[c] Jen-Chang Yang[d] and Aivaras Kareiva[e]

Received 17th January 2014,
Accepted 17th February 2014

DOI: 10.1039/c4ce00119b

www.rsc.org/crystengcomm

Previous synthesis routes created apatites in low crystallinity and high crystallinity states, but a wider range will extend the design capabilities of apatites for hard tissue replacements. While high crystallinity apatites are more conventional, this work investigated lower crystallinity variations from an amorphous state to low crystallinity apatite. Carbonated hydroxyapatite was prepared by precipitating an amorphous phase followed by crystallization at 650 °C at slow (5 °C min^{-1}) and fast heating rates (60 °C min^{-1}). The effect of processing conditions on crystallinity and structural changes was evaluated by thermal analysis, X-ray diffraction, transmission electron microscopy, Fourier transform infrared and Raman spectroscopy. Furthermore, peak deconvolution of IR and Raman spectra resolved the carbonate and phosphate bands and revealed the carbonate and crystalline phase content in CHAp. Similar to precipitation of crystalline apatites, the crystallization at elevated temperature led to carbonate in both the phosphate and hydroxyl positions. Heating at 650 °C provided a nanosized spherical hydroxyapatite containing carbonate controlled by the heating rate. This creates a mechanism for creating a large range in crystallinity with a greater resorption capability for regenerative medicine.

1. Introduction

The development of apatites for biomedical implants has evolved from sintered calcium hydroxyapatite ($Ca_{10}(PO_4)_6(OH)_2$, CHAp), but more recent work has been investigating apatites with a closer resemblance to that found in the body. One aspect involves adjusting the crystal size and the degree of structural order to more closely emulate the bone mineral. Secondly, the composition can be modified in the apatite structure to contain carbonate thereby providing a composition more similar to the bone mineral.

Carbonated calcium hydroxyapatite (CHAp) is found in the mineral component of natural bones and teeth and when the concentration of carbonate ions in the hydroxyapatite (HAp) lattice is in the range of 3–8 wt%.[1,2] Carbonate ions can substitute a hydroxide (OH^-) or phosphate (PO_4^{3-}) group, leading to A- or B-type carbonated apatites, respectively. The chemical formula for A-type carbonated apatites has been defined as $Ca_{10}(PO_4)_6(OH)_{2-2y}(CO_3)_y$, where $0 \leq y \leq 1$, while for the B-type $Ca_{10-x}(PO_4)_{6-x}(CO_3)_x(OH)_{2-x}$, where $0 \leq x \leq 2$ and sodium ions are located in the calcium sites, inducing a favourable electrical charge balance.[3–5] In biological apatites carbonate ions replace the PO_4^{3-} group and OH^- group and so can be considered as AB carbonate substituted apatites with the chemical formula of $Ca_{10-x}(PO_4)_{6-x}(CO_3)_x(OH)_{2-x-2y}(CO_3)_y$.[3,6,7]

Carbonated hydroxyapatite has been synthesized using precipitation,[2,3,8–10] sol–gel,[11,12] hydrothermal,[13–15] solid-state[16] and biomimetic processing.[17] It has been used as a filler in electrospun polycaprolactone fibres,[18] formed as coatings using pulsed laser deposition[19] or sol–gel[20] and as structural members in porous scaffolds.[21] The variety of preparation techniques provides possibilities to prepare CHAp in different forms (particles, porous bodies, and coatings) for implantation.

Biological activity of the bone mineral is strongly influenced by the amount of carbonate present in the apatite lattice. It has been demonstrated that CHAp is more soluble *in vivo* than pure HAp.[4,22] This has been attributed to structural defects arising from carbonate ions in the HAp lattice.[4,23] The mechanical properties of apatite ceramics can also be altered when carbonate ions are present in the lattice in comparison with those of pure HAp.[2,15,16,24]

[a] *Department of Applied Chemistry, Vilnius University, Naugarduko 24, LT-03225 Vilnius, Lithuania. E-mail: edita.garskaite@chf.vu.lt*
[b] *Institute of Biomaterials and Biomechanics, Azenes 14-201, LV-1048, Latvia. E-mail: Karlis-Agris.Gross@rtu.lv*
[c] *Department of Chemical Engineering and Biotechnology, National Taipei University of Technology, 1, Sec. 3, Chung-Hsiao E. Road, Taipei, 106, Taiwan*
[d] *Department of Dental Technology, Taipei Medical University, 250 Wu-Hsing str., Taipei, Taiwan*
[e] *Department of Inorganic Chemistry, Vilnius University, Naugarduko 24, LT-03225 Vilnius, Lithuania*

Crystallite shape is an important characteristic that has been given less emphasis, but this plays a large role in dictating the properties. In bone, a plate-like apatite is formed to fit into previously determined sites adjacent to the collagen chain and the crystal shape is important for imparting the required fracture properties. Most synthesis methods also provide a faceted geometry leading to beads, plates or cubes (Table 1). Techniques that do not involve crystal growth, such as sol–gel and amorphous precursors have the potential to obtain particles with a round-shape.

In bone the apatite is plate-like or needle-like.[25] Nevertheless, a variety of HAps having different morphologies and particle sizes were produced and integrated with collagen to mimic skeletal bones and optimize their mechanical properties.[25–28] A lot of attention has been given to delivery mechanisms of active ingredients for activating tissue growth, reducing infection and combating undesirable. The nanosize provides a larger surface area to form a greater drug loading capacity, and the spherical shape optimizes transportability.[29,30]

The availability to accommodate the carbonate in the A or B site provides a means of adjusting the properties. There is a greater tendency for carbonate to be placed in the phosphate site where the smaller size makes it easier for carbonate to fit into the lattice as opposed to the hydroxyl site where the larger size of carbonate will otherwise introduce a greater stress. Crystallization in solutions will be influenced by the lowest free energy state and so a B-type CHAp will be more likely. If the carbonate is kept in an amorphous state together with calcium and phosphate, then a slow transformation will also tend to reach a more stable state. If the amorphous phase can be dried and then crystallized at higher temperatures, then the sudden heating conditions and the positions of the carbonate in the amorphous state could affect the type of substitution that is formed. We hypothesize that carbonate placement in the lattice will be different at shorter heating times at crystallization when diffusion is not able to dictate positions for the lowest energy arrangement. The investigation will use both a slow and a rapid heating furnace to provide an accurate control of the heating schemes.

This work will investigate the preparation of a carbonated apatite with a crystal size similar to biological apatites. The objective of this work is to investigate whether lower crystallinity nanosized powders can be produced by thermal processing, thereby combining calcination and structure refinement within one processing step. Structure refinement involves the placement of the carbonate in the structure, the degree of order, and the crystal size. Heating will be conducted in a rapid heating and a conventional tube furnace to show the importance of heating rate and holding time on the crystallization of a carbonated hydroxyapatite.

2. Experimental part

2.1. Synthesis of the CHAp precursor

To synthesize the A-type carbonated apatite, a calcium nitrate tetrahydrate solution was mixed with a solution containing ammonium carbonate and diammonium hydrogen phosphate. The amorphous phase was washed with deionized water and then freeze dried. The amorphous phase will be herein referred to as the CHAp precursor. To calcine the CHAp precursor, two annealing schemes were used: I (fast annealing method) – the precursor was annealed at 650 °C (heating and cooling rate, 60 °C min^{-1}) for 1, 5 and 15 min, and II (slow annealing method) – the precursor sample was annealed at 650 °C (heating and cooling rate, 5 °C min^{-1}) for 5, 15 and 60 min.

Calcination scheme I was performed in a near-IR cold-wall rapid annealing furnace MILA-3000 (Ulvac/Sinku-Riko. Inc., Chigasaki, Japan) and scheme II in a quartz tube furnace. Annealing was performed in air in an alumina crucible or on an alumina plate (dimensions of the material ~1 × 0.5 × 0.5 cm^3).

Table 1 Particle characteristics (size, crystal shape and synthesis method) of carbonated apatites[a]

Synthesis method	Crystallite/particle size	Crystal shape	Measurement method	References
Hydrothermal (high pressure)	15 nm	Spherical	XRD	13
	90 × 50 μm			14
	1 μm	Plates/prisms	SEM	15
Precipitation	15 nm	Spherical	TEM	9
	18 × 4 nm	Needle-like		8
	50 × 61 nm	Spherical	XRD	10
	60 nm			3
	10 μm		Laser diffraction	2
Sol–gel	35 nm	Spherical	SEM	11
	1 μm	Plate-like		12
Sol–gel deposition	40 nm	Spherical	XRD	20
Self-assembly on collagen	21 nm (in fibrils)	Elongated		17
Electrospinning	240 nm	Spherical	SEM	18
Solid-state	—	μm domains		16
	20 nm	Spherical		21
Pulsed laser deposition	30 nm	—	XRD	19

[a] Note: the mean value has been provided to show the size.

2.2. Characterization

Thermogravimetric (TG) analysis, differential scanning calorimetry (DSC) and derivative thermogravimetric (DTG) analysis were performed on a Netzsch STA 449C Jupiter instrument from 26 to 1000 °C at a heating rate of 30 °C min^{-1} in air (initial sample mass was 23.3 mg).

X-ray diffraction was conducted on a PANalytical X'Pert PRO with a PW3050/60 goniometer using CuKα radiation generated at 45 kV and 40 mA. The diffracted signal was collected through a 1° divergence slit and a 2° anti-scatter slit for 5 seconds at a step size of 0.02° and over a 2θ range of 20–70°. Crystallite sizes were estimated by the Scherrer equation, $d_{XRD} = K\lambda/\beta \cos \theta$, using the full-width at half maximum (FWHM) of the (002), (202), (222), (203) and (004) Bragg reflections.

Infrared spectra were recorded on a Spectrum GX FTIR spectrometer (Perkin Elmer Inc.) using KBr pellets (prepared at 4000 psi). Samples were examined in transmission mode over the 400–4000 cm^{-1} range and an average was calculated from 32 scans.

Raman spectra were recorded using a Raman-Micro Raman and PL spectrometer equipped with a MonoRa 500i monochromator (DongWoo Optron Co., Ltd.) with an excitation source of 532 nm DPSS Laser (Omicron-Laserage Laserprodukte GmbH, Germany). The laser power at the sample was 80 mW. The spectra of three wavelength regions of 45–1295, 1350–2930 and 2535–3405 cm^{-1} were recorded under ambient conditions. IR and Raman peak fitting and deconvolution were carried out by the XPS PEAK software.

Elemental composition was investigated using a Hitachi S-3000H scanning electron microscope (SEM) at a 15 kV accelerating voltage using an energy dispersive X-ray spectrometer (EDX, Inca – Oxford Instruments).

Samples annealed in the quartz tube furnace were analysed by transmission electron microscopy (TEM): high-resolution TEM (HRTEM) and selected area electron diffraction (SAED). Powders were dispersed in ethanol in an ultrasonic bath (30 min) and a drop was placed on a 300 mesh Cu grid with holey carbon. TEM was conducted on Hitachi H-7100 (200 kV) and Philips/FEI Tecnai 20 G2 S-Twin (200 kV) transmission electron microscopes.

3. Results and discussion

3.1. Thermal analysis

The crystallization temperature of the CHAp precursor was evaluated from thermal analysis. TG/DTG/DSC curves presented in Fig. 1 show that heating at 100 °C resulted in an 8.6% weight loss from the release of adsorbed water. An additional weight loss of 46.2% occurred upon further heating up to 600 °C following a strong exothermic peak at ~630 °C. This loss was attributed to the removal from the surface (ammonium and water) and the lattice (water and carbonate). Heating to 750 °C produced an additional 2.4% weight loss and the step up to 900 °C provided a further 2.5% decrease in weight. This was also assigned to the removal of the lattice

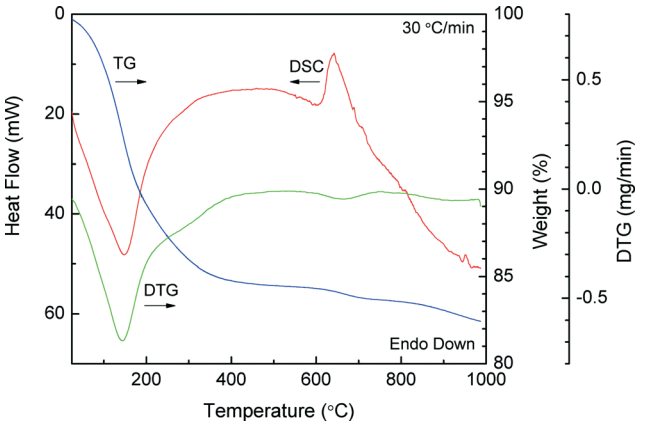

Fig. 1 TG/DTG and DSC analysis curves of the CHAp precursor showing a continual weight loss upon heating, but crystallization at 650 °C.

water and the possible release of carbonate from the A-site in the lattice along the columns.[31,32] It is known that heating of apatites at higher temperatures can lead to dehydroxylation. Skinner *et al.*[33] demonstrated that dehydroxylation of HAp starts above 700 °C. To prevent changes in the composition, a sintering temperature of 650 °C was chosen.

3.2. Crystallization

The crystallization depends on the heating rate up to the holding temperature. Heating at 60 °C min^{-1} produced crystallization only after 15 minutes of annealing (Fig. 2). The crystalline peaks arise from the Bragg diffraction conditions for HAp (JCPDS no. 09-0432, hexagonal crystal system, space group of $P6_3/m$). Longer annealing times increased the crystallinity.

The XRD patterns of samples after heating at 5 °C min^{-1} (Fig. 3) show crystalline powders – Bragg reflections matched well with the pattern of HAp. No impurity phases were observed.

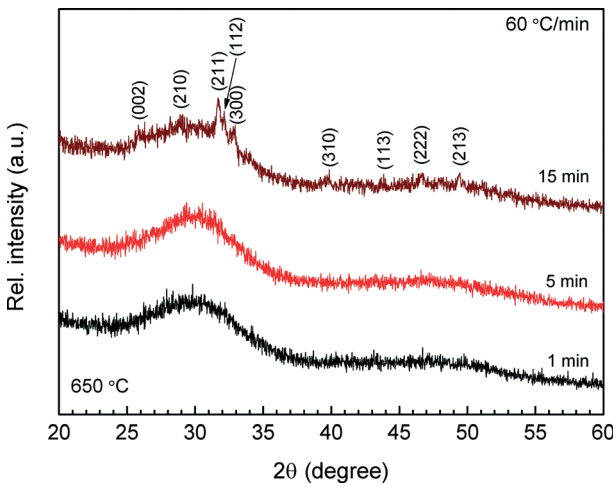

Fig. 2 XRD patterns of CHAp precursor samples heated at 60 °C min^{-1} and held at 650 °C for 1, 5 and 15 min show slow crystallization for rapidly heated powders.

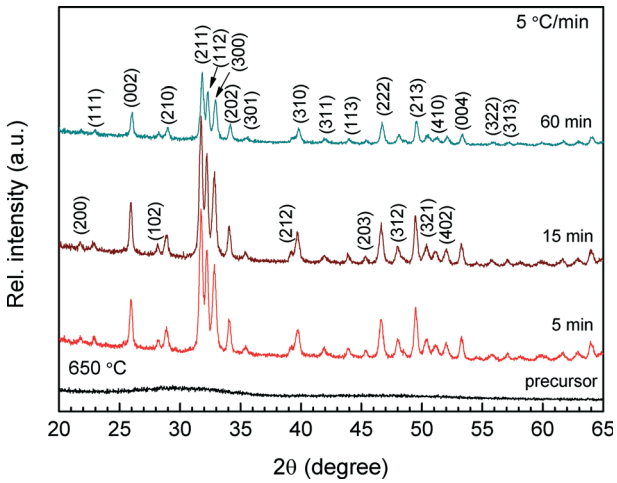

Fig. 3 XRD patterns of CHAp precursor powders heated at 5 °C min^{-1} to 650 °C and held for 5, 15 and 60 min show ease of crystallization for slowly heated samples.

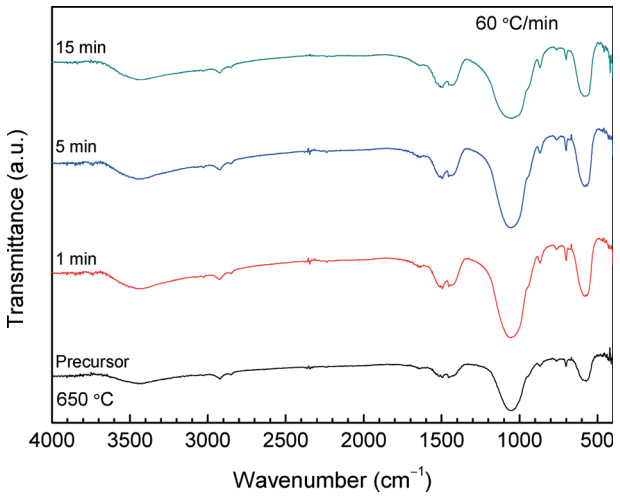

Fig. 4 IR spectra of CHAp precursor samples after heating at 60 °C min^{-1} and held at 650 °C for 1, 5 and 15 min do not show clear changes in the bonding.

Difference in crystallinity for the two sets of samples can be explained in terms of the heating rate which will influence the nucleation and hence the crystallization. Milev *et al.*[12] investigated the crystallization kinetics of HAp where a direct relationship between the heating rate and the crystallization temperature was shown. It was demonstrated that increasing the heating rate from 5 to 40 K min^{-1} raised the crystallization temperature by 50 °C, from 805 to 854 K.

Average crystallite sizes of samples calcined for 5, 15 and 60 min (annealing scheme II) were calculated from the X-ray diffraction patterns to be 37, 39 and 40 ± 5 nm, respectively. This shows that once the crystal zone is established, further growth is not expected, reflecting the lack of diffusion at 650 °C. The size of nucleated primary particles of the amorphous calcium phosphate may determine the crystal size.

3.3. Bond development through spectroscopy

IR spectra of the precursor and samples annealed at a fast heating rate are presented in Fig. 4, and the assignment of the bands is summarized in Table 2. The broad absorption bands in the regions of 1190–900 cm^{-1} and 635–530 cm^{-1} are due to the apatitic PO_4^{3-} groups: the former comes from a triply degenerate asymmetric stretching mode, ν_3, and a symmetric stretching mode, ν_1, of the P–O bonds, while the latter from a triply degenerate bending mode, ν_4, of the O–P–O bonds.[34] Bands in the 1550–1280 cm^{-1} region are characteristic of the carbonate (CO_3^{2-}) group. A band located at 1494 cm^{-1} was assigned to the stretching mode, ν_3, while bands at 1454 and 1436 cm^{-1} to the bending modes, ν_4 or ν_3, of the C–O bond. In addition, a band arising from the bending mode, ν_2, of the C–O bond (CO_3^{2-} group) was also observed at ~868 cm^{-1}. Furthermore, in the spectra weak bands located at ~761 and 701 cm^{-1} were observed and attributed to the vibrations of CO_3^{2-} moieties of $CaCO_3$ (ν_4, in-plane band). According to Andersen and Brecevic,[35] in the FTIR spectra of the amorphous form of vaterite, one of the characteristic absorption bands is located at ~744 cm^{-1} (ν_4). This absorption band could shift to 761 cm^{-1} due to the different crystalline structures between apatite and calcium carbonate.

Table 2 IR band assignment of the samples annealed using a heating/cooling rate of 60 °C min^{-1}[a]

Wavenumber (cm^{-1})					
	Annealing scheme I				
Precursor	1 min	5 min	15 min	Peak assignment	References
1494 (m)	1496 (m)	1494 (m)	1495 (m)	ν_3 stretching mode of the CO_3^{2-} in CAP	2,34
1453 (m)	1454 (m), 1436 (sh)	1454 (m), 1436 (sh)	1454 (m), 1436 (sh)	ν_4 or ν_3 bending mode of the CO_3^{2-} (C–O bond) in A- and B-type CAP and ν_1 stretching mode of CO_3^{2-} (C–O bond) in B-type CAP	2,34
1050 (vs)	1050 (vs)	1051 (vs)	1047 (vs)	ν_{3b} triply degenerate asymmetric stretching mode of PO_4^{3-} (P–O bond)	34
940 (sh)	940 (sh)	940 (sh)	940 (sh)	ν_1 nondegenerate symmetric stretching mode of PO_4^{3-} (P–O bond)	34
869 (m)	867 (m)	868 (m)	869 (m)	ν_2 bending mode of CO_3^{2-} (C–O bond) in CAP	34
762 (w)	760 (w)	762 (w)	762 (w)	ν_4 in-plane deformation bending mode of CO_3^{2-} (O–C–O bond)	35
701 (m)	701 (m)	701 (m)	701 (m)	ν_4 in-plane deformation bending mode of CO_3^{2-} (O–C–O bond)	35
583 (572) (s), 567 (s)	581 (s), 567 (s)	581 (s), 567 (s)	579 (s), 568 (s)	ν_4 triply degenerate bending mode of PO_4^{3-} (O–P–O bonds)	15,34

[a] m: medium, s: strong, sh: shoulder, v: very, w: weak.

IR spectra of crystallized apatites annealed using the slow annealing scheme are shown in Fig. 5 and listed in Table 3. Contrary to the above spectra, here the PO_4^{3-} bands representing apatite are split into several more narrow bands. Rehman and Bonfield[36] have investigated CHAp and five (synthesised and commercial) HAp samples using IR spectroscopy and showed that bands characteristic of the HAp are difficult to distinguish from CHAp.

In the 900–1190 cm^{-1} region, bands located at ~1084, 1034 and 960 cm^{-1} were obtained (triply degenerate asymmetric stretching mode, v_3, and symmetric stretching mode, v_1, of the P–O bonds), as well as in the low wavenumber region at 602 and 571 cm^{-1} (triply degenerate bending, v_4, mode of the O–P–O bonds). Furthermore, two distinctive peaks observed at 3570 and 632 cm^{-1} were assigned to the stretching mode, v_s, and the vibrational mode, v_L, of the structural hydroxyl anion (OH^-) in HAp, respectively.

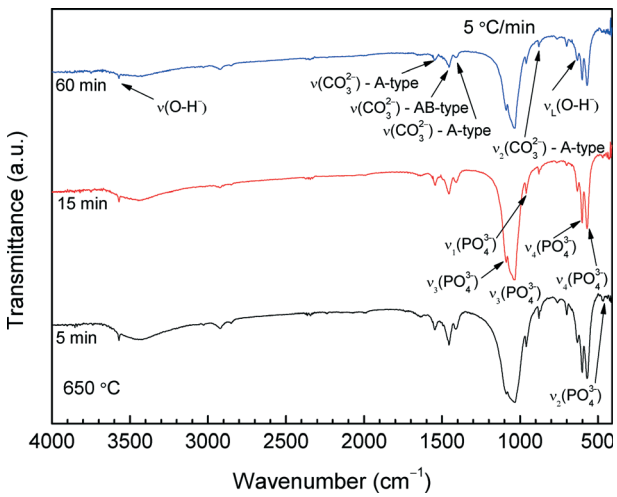

Fig. 5 IR spectra of the CHAp precursor after heating at 5 °C min^{-1} and held at 650 °C for 5, 15 and 60 min show sharp peaks corresponding to carbonated hydroxyapatite.

Bands corresponding to the CO_3^{2-} group were also detected. Those located at 1544 and 879 cm^{-1} represent CO_3^{2-} anions partially occupying OH^- positions (A-type), while the bands detected at 1455 and 1409 cm^{-1} reflect partial PO_4^{3-} substitution (B-type).[14,34] Similar results were obtained by Neira *et al.*[15] where CHAp was produced using hydrothermal synthesis. The ratio of the extinction of the 1546 cm^{-1} band (A-type CO_3^{2-}) to that of the 1413 cm^{-1} band (B-type CO_3^{2-}) can roughly show the content of A- and B-type CO_3^{2-}.[37] The spectra demonstrate that these bands are similar with the intensity slightly higher for the band corresponding to the A-type CO_3^{2-}. This shows that A- and B-type substitution occurred simultaneously and AB-type CHAp was formed. Furthermore, as in previous spectra the bands located at ~761 and 701 cm^{-1} were also observed. A broad band at 3440 cm^{-1} as well as one at 1640 cm^{-1} observed in all of the spectra were assigned to the adsorbed H_2O.[34]

The finding on carbonate placement answers the hypothesis by showing that a lower energy condition is achieved by distribution of the carbonate to both positions, and not solely to the B position. Both crystal formation in aqueous solutions and higher temperature crystallization (as shown here) show carbonate distribution to both sites.

For more detailed analysis, an algorithmic curve fit and the component peaks were determined for the IR spectra (1300–800 cm^{-1} region) produced from slowly heated samples (scheme II) (Fig. 6). Nine individual peaks were used. Peaks at 1100, 1065 and 1034 cm^{-1} were labelled as A, B and C bands.

According to the study by Pleshko *et al.*,[38] there is a correlation between band area, position and crystallite size: the fractional intensity of the band around 1057–1067 cm^{-1} in the FT-IR spectra decreases with an increase in the crystal size for biological apatites within a size range of 100–200 Å.

Table 3 IR band assignment of the samples annealed using a heating/cooling rate of 5 °C min^{-1}[a]

Wavenumber (cm^{-1})				
Annealing scheme II				
5 min	15 min	60 min	Peak assignment	References
3570 (w)	3570 (w)	3571 (w)	v_s stretching mode of O–H	15,34
1546 (m)	1544 (m)	1547 (m)	v_4 bending mode of CO_3^{2-} (A-type)	2,14,15,34
1494 (vw/sh)	1497 (vw/sh)	1497 (vw/sh)	v_3 stretching mode of CO_3^{2-} in CAP (A-type of B-type)	2,34
1455 (s)	1455 (s)	1455 (s)	v_3 or v_4 bending mode of CO_3^{2-} (A- and B-type)	2,14,36
1413 (m)	1409 (m)	1408 (m)	v_3 stretching mode of CO_3^{2-} (B-type)	2,14,34,36
1088 (s)	1089 (s)	1089 (s)	v_{3a} triply degenerate asymmetric stretching mode of PO_4^{3-} (P–O bond)	34,36
1034 (vs)	1037 (vs)	1036 (vs)	v_{3c} triply degenerate asymmetric stretching mode of PO_4^{3-} (P–O bond)	34
961 (m)	961 (m)	961 (m)	v_1 nondegenerate symmetric stretching mode of PO_4^{3-} (P–O bond)	34,36
879 (m)	879 (m)	880 (m)	v_2 bending mode of CO_3^{2-} (A-type)	14,15,34,36
759 (w)	764 (w)	764 (w)	v_4 in-plane deformation bending mode of CO_3^{2-} (O–C–O bond)	35
700 (m)	700 (m)	701 (m)	v_4 in-plane deformation bending mode of CO_3^{2-} (O–C–O bond)	35
633 (m)	633 (m)	632 (m)	v_L librational mode of OH (O–H bond)	15,34
602 (s)	602 (s)	602 (s)	v_{4a} triply degenerate bending mode of PO_4^{3-} (O–P–O bond)	34,36
571 (s)	571 (s)	570 (s)	v_{4b} triply degenerate bending mode of the PO_4^{3-} (O–P–O bond)	34,36
466 (vw)	466 (vw)	466 (vw)	v_2 doubly degenerate bending mode of PO_4^{3-} (O–P–O bond)	34

[a] CAP – carbonated apatite.

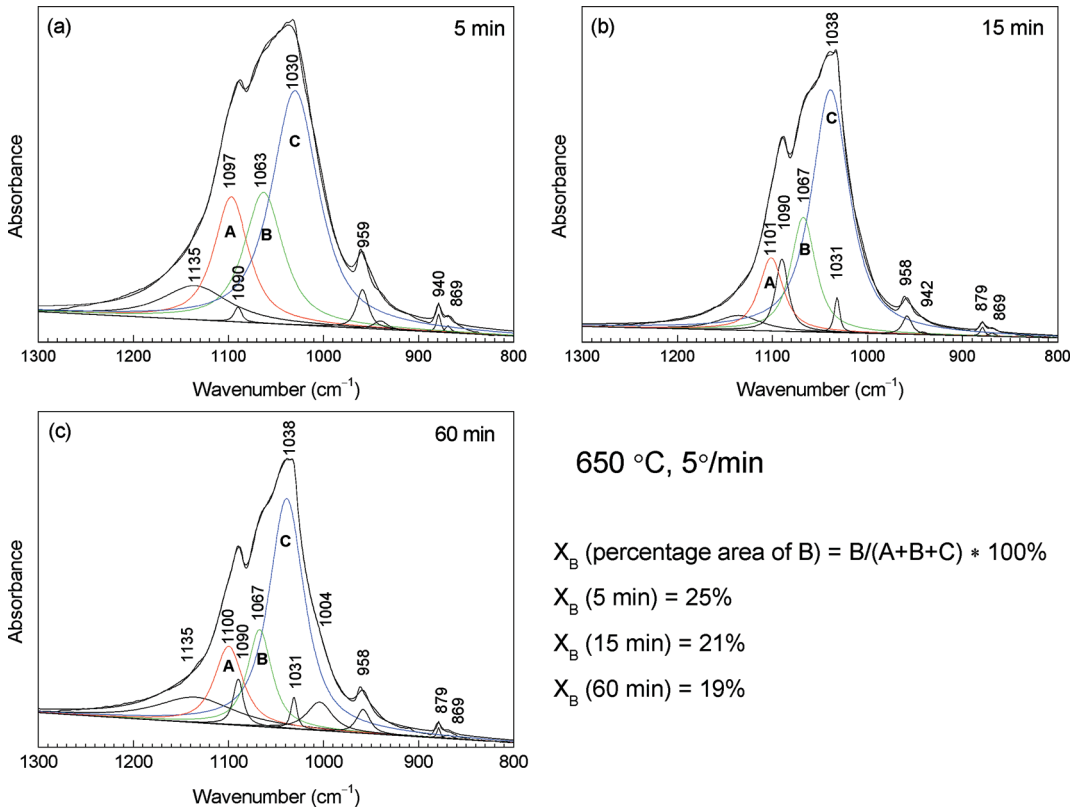

Fig. 6 IR peak deconvolution of the CHAp precursor after heating at 5° min^{-1} and held at 650 °C for (a) 5 min, (b) 15 min and (c) 60 min.

The percentage area of band B was calculated to be 25, 21 and 19% for samples annealed for 5, 15 and 60 min, respectively, when A + B + C was 100%. When the area of all peaks totalled to 100%, the percentage area of component B was 22, 18 and 14%. This is in agreement with data obtained from XRD analysis where it was found that the particle size slightly increases with an increase of the annealing temperature. In order to obtain a better algorithmic fit, the small bands at about 1090, 1031 and 1004 cm^{-1} were also defined. Bands are due to the presence of PO_4^{3-} or CO_3^{2-} groups.[34] The intensity and sharpness of these bands increase with an increase of the annealing time, and this is directly related to the increased crystallinity (a greater order in the lattice and a larger amount of crystalline phase).[39] Furthermore, IR spectra in the region of 1200–900 cm^{-1} have a well defined peak at 959 cm^{-1} which also is correlated with a higher crystallinity of apatites.[38]

Raman spectra of an amorphous precursor annealed powder showed the course of crystallization at a slow heating rate (Fig. 7). In the spectrum of an amorphous precursor, the band located at 952 cm^{-1} (Fig. 7(a)) was assigned to the vibrations of the PO_4^{3-} group,[40] and the weak and broad bands of ν_3 (1985–1970 cm^{-1}), ν_4 (650–540 cm^{-1}) and ν_2 (500–400 cm^{-1}) modes of the PO_4^{3-} group are characteristic of amorphous calcium phosphate.[40,41] Carbonate bands in the Raman spectra are very weak due to its low concentration. In the spectra of calcined samples (Fig. 7(b)–(d)), the most intense band at 962 cm^{-1} is assigned to the ν_1 mode of the PO_4^{3-} group for crystalline HAp. The PO_4^{3-} bands were also observed in the 430–450 cm^{-1} region (bending modes, ν_2 and ν_4, of the O–P–O bond), at 595 cm^{-1} (bending mode, ν_4, of the O–P–O bond), and in the 1085–1040 cm^{-1} region (asymmetric stretching mode, ν_3, of the P–O bond).[34] It is also worthwhile to note that the broad band obtained at 1074 cm^{-1} most likely consists of two overlapped bands located at 1078 cm^{-1} and at 1071 cm^{-1} owing to the ν_3 mode of the PO_4^{3-} group and to the ν_1 mode of the CO_3^{2-} group (B-type substitution), respectively.[42,43]

More detailed information was available from the peak deconvolution. The 1095–1060 cm^{-1} region was resolved to two component peaks. 92% of the original band area was attributed to the PO_4^{3-} group (1078 cm^{-1}) while 8% to the CO_3^{2-} group (1071 cm^{-1}). The FWHM of the band located at 962 cm^{-1} was 10.52 cm^{-1}. According to Avonusi *et al.*[42] and the presented trend that combines peak widths as a function of carbonate content, the calculated FWHM might correspond to 4.5 ± 0.5 wt% of carbonate in the sample. Furthermore, the band located at 1107 cm^{-1} is a characteristic signature of A-type substitution in HAp and is assigned to the ν_1 mode of the CO_3^{2-} group.[43] Raman spectra analysis supports previously described IR spectra confirming that AB-CHAp has been synthesized when samples were calcined using the slow annealing scheme. The assignment of all obtained bands in Raman spectra is summarised in Table 4.

Powders heated at a fast heating rate show that the band of vibrations characteristic of the PO_4^{3-} group was shifted to

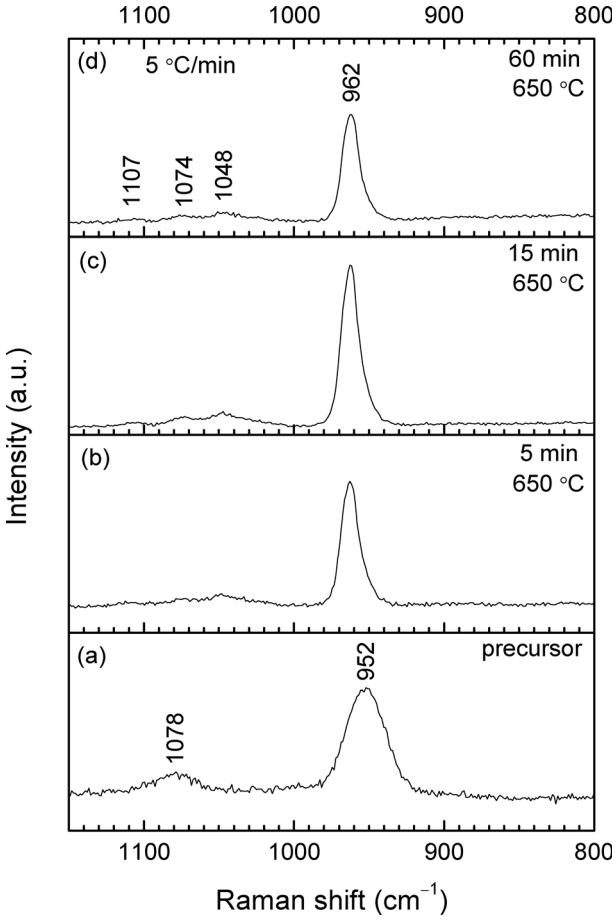

Fig. 7 Raman spectra of the precursor sample (a) and CHAp samples after heating at 5° min^{-1} and held at 650 °C for 5 (b), 15 (c) and 60 min (d).

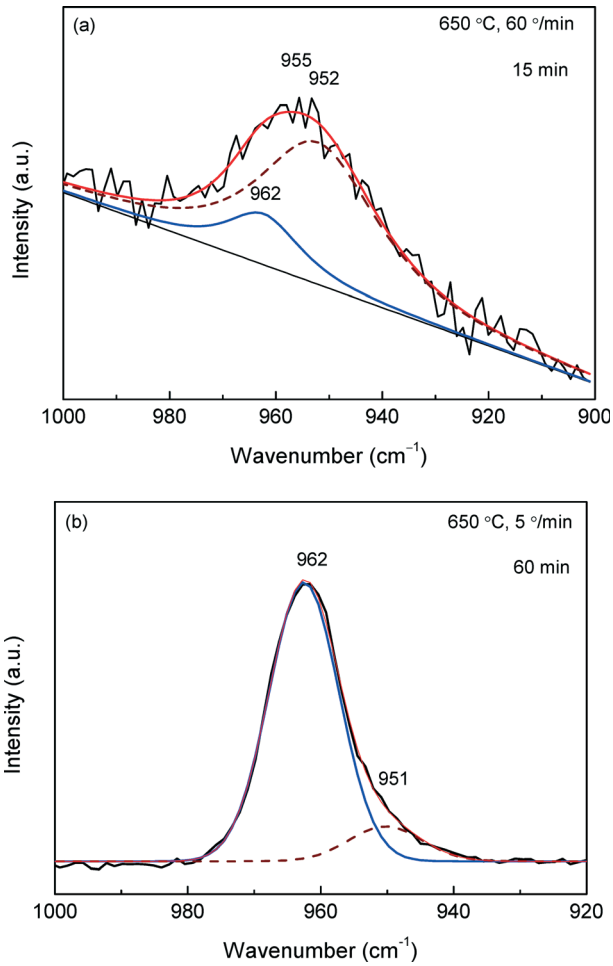

Fig. 8 Raman spectra with peak deconvolution of CHAp samples heated at (a) 60 °C min^{-1} and held at 650 °C for 15 min (shows the appearance of the crystalline component from the 962 peak) and (b) at 5 °C min^{-1} and held at 650 °C for 15 min.

higher wavenumbers (955 cm^{-1}). This is ascribed to partial crystallization of the powder.[44] The shift and changes in the FWHM of the characteristic band of the PO_4^{3-} group were shown by Ou-Yang *et al.*[45] when the maturation of HAp from amorphous apatite was investigated. The spectra also exhibited very weak and broad bands located in the regions of 1120–1960 cm^{-1} and 490–430 cm^{-1}. The former is assigned to the overlapping bands arising from vibrations of the PO_4^{3-} and CO_3^{2-} groups, while the latter to the ν_3 and ν_4 modes of the PO_4^{3-} group.[43]

In order to see the content of the crystalline phase, deconvolution of the band located at 955 cm^{-1} in all of the Raman spectra of the samples annealed using the fast annealing scheme was performed. Two components were chosen corresponding to amorphous apatite (952 cm^{-1}) and to the crystalline HAp (962 cm^{-1}) phases. The values

Table 4 Raman spectra assignment[a]

Wavenumber (cm^{-1})				
Amorphous precursor	Samples (annealing scheme I)	Samples (annealing scheme II)	Peak assignment	References
—	1096 (vw)	1107 (vw)	ν_1 symmetric stretching mode of CO_3^{2-} (A-type)	42,43
1078 (m)		1074 (w), 1048 (m)	ν_3 triply degenerate asymmetric stretching mode of PO_4^{3-} (P–O bond) and ν_1 symmetric stretching mode of CO_3^{2-}	34,42
953 (vs)	955 (m)	962 (vs)	ν_1 nondegenerate symmetric stretching mode of PO_4^{3-} (P–O bond)	34
600 (m)	598 (vw)	595 (m)	ν_4 triply degenerate bending mode of PO_4^{3-} (O–P–O bond)	34
449 (m),	449 (vw)	449 (m),	ν_4 triply degenerate bending mode of PO_4^{3-} (O–P–O bond)	43
434 (m)	433 (vw)	434 (m)	ν_2 doubly degenerate bending mode of PO_4^{3-} (O–P–O bond)	34,43

[a] m: medium, s: strong, v: very, w: weak.

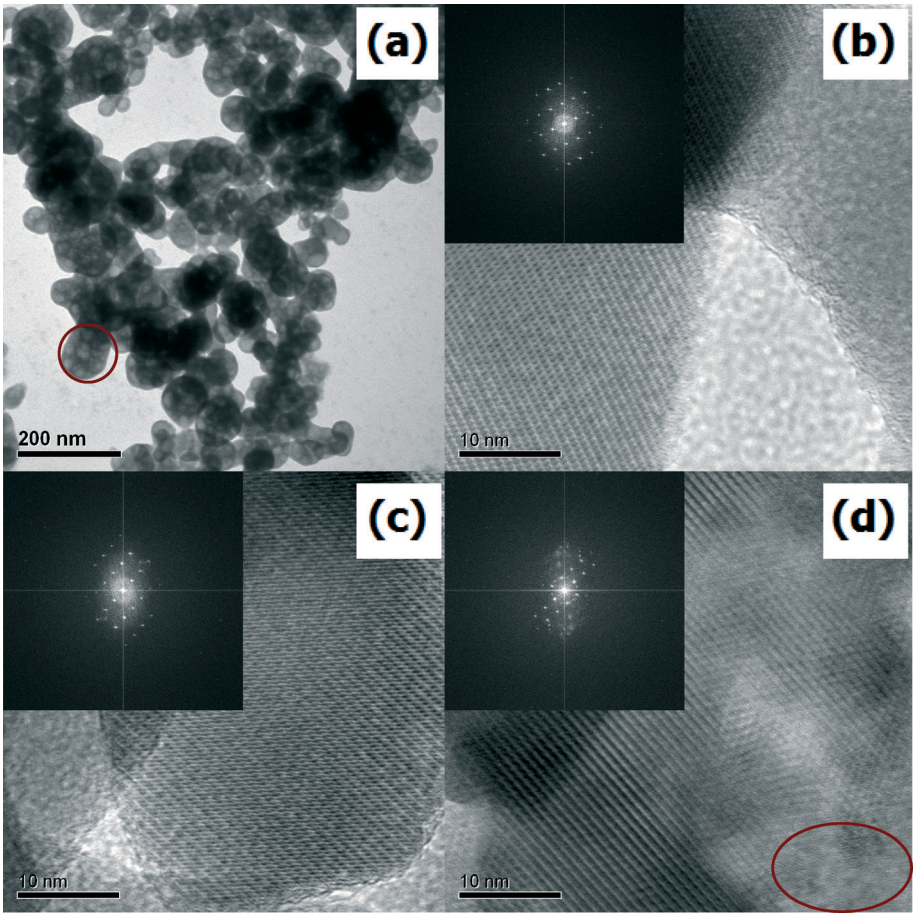

Fig. 9 TEM images of (a) the precursor sample (marked nucleated primary particles) and CHAp samples after heating at 5 °C min^{-1} and held at 650 °C for (b) 5 min, (c) 15 min and (d) 60 min (marked defective region). Insets: SEAD patterns.

determined by band deconvolution are as follows: 93% and 7%, 93% and 7%, and 82% and 18% for the samples annealed for 1, 5 and 15 min, respectively. A slight increase in the crystalline phase with increasing annealing time was observed. The Raman spectrum and deconvolution of the 955 cm^{-1} band of sample annealed for 15 min is presented in Fig. 8(a).

Band deconvolution was performed on all samples annealed using slow annealing scheme. Fig. 8(b) shows the Raman spectrum and deconvolution of the 962 cm^{-1} band of the sample annealed for 60 min. Performed band fitting gave two components corresponding to the amorphous (952–950 cm^{-1}) and crystalline (963–962 cm^{-1}) phases of apatite. Percentage values of these components are: 86% and 14%, 88% and 11%, and 88% and 11% for samples annealed for 5, 15 and 60 min, respectively. Results show that prolonging the annealing time up to 60 min did not significantly reduce the amorphous phase content in this set of samples. This may be related to the effect of hydroxyl vacancy on the phosphate vibration.

3.4. TEM analysis

TEM analysis of the precursor and three calcined samples using the slow annealing scheme showed crystallization of nucleated primary particles (Fig. 9). We observed that samples calcined using the fast annealing regime tend to shrink when exposed to the electron beam. This could be related to the removal of ammonia, nitrate or adsorbed water. HR-TEM and SAED results showed that all of the samples heated at 5 °C min^{-1} to 650 °C are crystalline with a small degree of defects obtained in the crystal lattice (Fig. 9(d)), assigned to the amorphous phase of apatite. This also supports the findings from the Raman analysis that reveal an 11–14% from a disordered structure – amorphous calcium phospate.

Particle size from TEM image analysis was estimated to be ~40 nm, which agrees with XRD analysis findings.

To understand the effect of all of the heating parameters on crystallinity, additional experiments were conducted to determine the contribution of the cooling rate. Powders heated at 10 °C min^{-1} to the desired temperature and then immediately cooled at a slow rate (180 minutes in the conventional furnace) and a fast rate (30 minutes in the rapid heating furnace) showed that a slower cooling rate provided more time for crystallization of the amorphous calcium phosphate. The contribution of the heating and cooling rates thus collectively determined the final crystallinity of the heated powder.

These studies showed that CHAp nanopowders of the AB-type can be processed at temperatures as low as 650 °C.

The degree of crystallinity (amount of amorphous and crystalline phases) can be regulated by adjusting the annealing conditions (heating rate and holding time). Crystals grow to the perimeter of the cluster and so changing the cluster size will also facilitate a change in the crystal size. Furthermore, results showed that incorporation of carbonate into the different sites of the HAp lattice is also induced by changing these processing parameters. The finer ability to design carbonated apatites will open up a wider choice of materials for use in biomedical implants.

4. Conclusions

The AB-type carbonated hydroxyapatite (CHAp) was produced by crystallization of a carbonate containing amorphous calcium phosphate. Two annealing schemes of 5 °C min^{-1} (slow annealing scheme) and 60 °C min^{-1} (fast annealing scheme) were compared. According to XRD and TEM analyses, crystalline CHAp samples were obtained more readily at a slower heating rate of 5 °C min^{-1} to 650 °C, giving an average crystallite size of 38 ± 5 nm. Less crystallization occurred at a higher heating rate. The resulting carbonated apatite contained carbonate in both phosphate and hydroxyl positions similar to apatite crystallized in solution, but with a spherical shape and better control over crystallinity.

Acknowledgements

This work is partly supported by the Taiwan–Latvia–Lithuania Foundation for Scientific Cooperation within the project "Nanoscaled functional materials for biotechnological and optical applications", no. IZM 11-13-0501/21 and by the European Community's Social Foundation under grant agreement no. VP1-3.1-_SMM-08-K-01-004/KS-120000-1756. KAG was supported by the Marie Curie reintegration grant, PIRG05-GA-2009-249306.

References

1 S. Bose and S. Tarafder, *Acta Biomater.*, 2012, **8**, 1401–1421.
2 J. C. Merry, I. R. Gibson, S. M. Best and W. Bonfield, *J. Mater. Sci.: Mater. Med.*, 1998, **9**, 779–783.
3 J. P. Lafon, E. Champion and D. Bernache-Assollant, *J. Eur. Ceram. Soc.*, 2008, **28**, 139–147.
4 E. Kovaleva, M. Shabanov, V. Putlyaev, Y. Tretyakov, V. Ivanov and N. Silkin, *Cent. Eur. J. Chem.*, 2009, **7**, 168–174.
5 M. Vallet-Regí and D. A. Arcos Navarrete, in *Biomimetic Nanoceramics in Clinical Use: From Materials to Applications*, The Royal Society of Chemistry, 2008, pp. 1–24.
6 J. C. Elliott, R. M. Wilson and S. E. P. Dowker, *Adv. X-Ray Anal.*, 2002, **45**, 172–181.
7 T. Leventouri, *Biomaterials*, 2006, **27**, 3339–3342.
8 S. Padilla, I. Izquierdo-Barba and M. Vallet-Regí, *Chem. Mater.*, 2008, **20**, 5942–5944.
9 J. E. Barralet, S. M. Best and W. Bonfield, *J. Mater. Sci.: Mater. Med.*, 2000, **11**, 719–724.
10 A. J. Melville, J. Harrison, K. A. Gross, J. S. Forsythe, A. O. Trounson and R. Mollard, *Biomaterials*, 2006, **27**, 615–622.
11 P. Layrolle, A. Ito and T. Tateishi, *J. Am. Ceram. Soc.*, 1998, **81**, 1421–1428.
12 A. Milev, G. S. K. Kannangara and B. Ben-Nissan, *Mater. Lett.*, 2003, **57**, 1960–1965.
13 V. Jokanović, D. Izvonar, M. Dramićanin, B. Jokanović, V. Živojinović, D. Marković and B. Dačić, *J. Mater. Sci.: Mater. Med.*, 2006, **17**, 539–546.
14 M. E. Fleet and X. Liu, *J. Solid State Chem.*, 2004, **177**, 3174–3182.
15 I. S. Neira, Y. V. Kolen'ko, O. I. Lebedev, G. Van Tendeloo, H. S. Gupta, F. Guitián and M. Yoshimura, *Cryst. Growth Des.*, 2008, **9**, 466–474.
16 I. R. Gibson and W. Bonfield, *J. Biomed. Mater. Res.*, 2002, **59**, 697–708.
17 S. Liao, F. Watari, M. Uo, S. Ohkawa, K. Tamura, W. Wang and F. Cui, *J. Biomed. Mater. Res., Part B*, 2005, **74**, 817–821.
18 P. Wutticharoenmongkol, N. Sanchavanakit, P. Pavasant and P. Supaphol, *Macromol. Biosci.*, 2006, **6**, 70–77.
19 J. V. Rau, A. Generosi, S. Laureti, V. S. Komlev, D. Ferro, S. N. Cesaro, B. Paci, V. R. Albertini, E. Agostinelli and S. M. Barinov, *ACS Appl. Mater. Interfaces*, 2009, **1**, 1813–1820.
20 A. H. Rajabi-Zamani, A. Behnamghader and A. Kazemzadeh, *Mater. Sci. Eng., C*, 2008, **28**, 1326–1329.
21 E. Landi, G. Celotti, G. Logroscino and A. Tampieri, *J. Eur. Ceram. Soc.*, 2003, **23**, 2931–2937.
22 Y. Doi, T. Shibutani, Y. Moriwaki, T. Kajimoto and Y. Iwayama, *J. Biomed. Mater. Res.*, 1998, **39**, 603–610.
23 A. Porter, N. Patel, R. Brooks, S. Best, N. Rushton and W. Bonfield, *J. Mater. Sci.: Mater. Med.*, 2005, **16**, 899–907.
24 R. I. Martin and P. W. Brown, *J. Mater. Sci.: Mater. Med.*, 1995, **6**, 138–143.
25 J.-Y. Rho, L. Kuhn-Spearing and P. Zioupos, *Med. Eng. Phys.*, 1998, **20**, 92–102.
26 A. Tampieri, G. Celotti, E. Landi, M. Sandri, N. Roveri and G. Falini, *J. Biomed. Mater. Res., Part A*, 2003, **67**, 618–625.
27 E. Landi, A. Tampieri, G. Celotti, R. Langenati, M. Sandri and S. Sprio, *Biomaterials*, 2005, **26**, 2835–2845.
28 D. A. Wahl and J. T. Czernuszka, *Eur. Cells Mater.*, 2006, **11**, 43–56.
29 M.-Y. Ma, Y.-J. Zhu, L. Li and S.-W. Cao, *J. Mater. Chem.*, 2008, **18**, 2722–2727.
30 H. Ong, J. C. Loo, F. C. Boey, S. Russell, J. Ma and K.-W. Peng, *J. Nanopart. Res.*, 2008, **10**, 141–150.
31 K. Tõnsuaadu, K. Gross, L. Plūduma and M. Veiderma, *J. Therm. Anal. Calorim.*, 2011, 1–13.
32 K. Tőnsuaadu, M. Peld and V. Bender, *J. Therm. Anal. Calorim.*, 2003, **72**, 363–371.
33 H. C. W. Skinner, J. S. Kittelberger and R. A. Beebe, *J. Phys. Chem.*, 1975, **79**, 2017–2019.
34 S. Koutsopoulos, *J. Biomed. Mater. Res.*, 2002, **62**, 600–612.
35 F. A. Andersen and L. Brecevic, *Acta Chem. Scand.*, 1995, **45**, 1018–1024.
36 I. Rehman and W. Bonfield, *J. Mater. Sci.: Mater. Med.*, 1997, **8**, 1–4.

37 G. Xu, I. A. Aksay and J. T. Groves, *J. Am. Chem. Soc.*, 2001, **123**, 2196–2203.
38 N. Pleshko, A. Boskey and R. Mendelsohn, *Biophys. J.*, 1991, **60**, 786–793.
39 L. M. Miller, V. Vairavamurthy, M. R. Chance, R. Mendelsohn, E. P. Paschalis, F. Betts and A. L. Boskey, *Biochim. Biophys. Acta, Gen. Subj.*, 2001, **1527**, 11–19.
40 M. Kazanci, P. Fratzl, K. Klaushofer and E. P. Paschalis, *Calcif. Tissue Int.*, 2006, **79**, 354–359.
41 H. Li, B. S. Ng, K. A. Khor, P. Cheang and T. W. Clyne, *Acta Mater.*, 2004, **52**, 445–453.
42 A. Awonusi, M. Morris and M. Tecklenburg, *Calcif. Tissue Int.*, 2007, **81**, 46–52.
43 G. Penel, G. Leroy, C. Rey and E. Bres, *Calcif. Tissue Int.*, 1998, **63**, 475–481.
44 C. Combes and C. Rey, *Acta Biomater.*, 2010, **6**, 3362–3378.
45 H. Ou-Yang, E. P. Paschalis, A. L. Boskey and R. Mendelsohn, *Biopolymers*, 2000, **57**, 129–139.